Microquasars as High Energy Gamma-ray Sources

Masaki Mori

Reference:

G. E. Romero, Chin. J. Astron. Astrophys. Vol.5 (2005), Suppl., 110-120

J. M. Paredes, Chin. J. Astron. Astrophys. Vol.5 (2005), Suppl., 121-132

H.E.S.S. astro-ph/0607192 ; MAGIC Science 312 (2006) 1771

ICRR CANGAROO Group Internal Seminar, 20-JUL-2006

Microquasars

- X-ray binaries with relativistic radio jets
- X-ray binaries

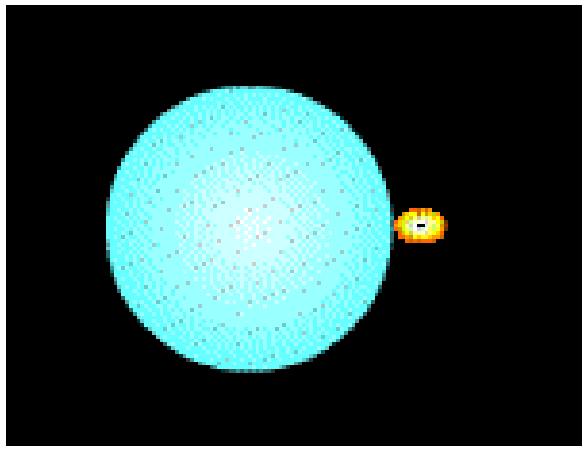

~130 HMXBs (High Mass X-ray Binaries)

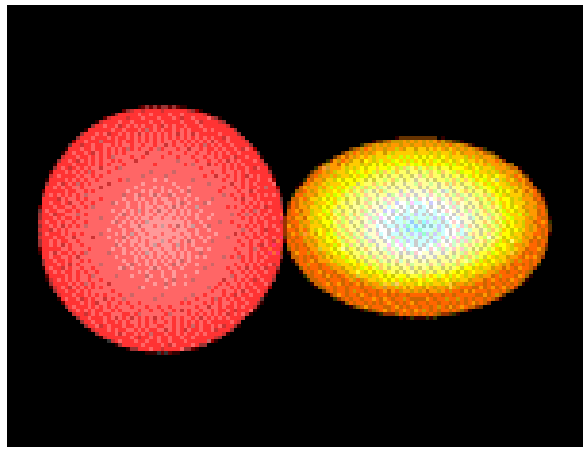

~150 LMXBs (Low Mass X-ray Binaries)

- 15 Microquasars (as of 2004)

http://www.physics.usyd.edu.au/~kuncic/

GRS 1915+105

Example:

Galactic microquasar GRS 1915+105 was the first superluminal source detected in the Galaxy. The radio images here show a pair of blobs expelled from the centre (yellow cross). The brighter blob on the left has an apparent transverse speed $\beta_T \simeq 1.25$. The actual speed of the blobs is $\beta \simeq 0.92$, with $\theta \simeq 70^\circ$.

(Mirabel & Rodriguez 1998, *Nature*, 392, 673)

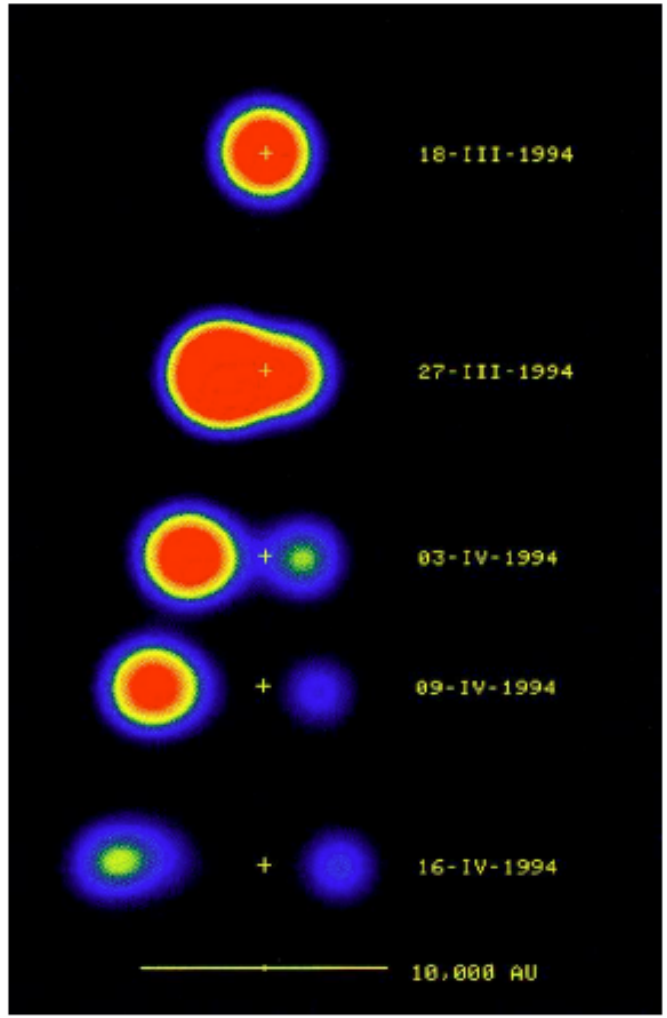

Superluminal motion

In some cases the inferred speeds of bright jet knots are superluminal. Apparent superluminal motion arises when the emitting ejecta are moving at ultra-relativistic speeds, so they almost catch up to the radiation they are emitting. Consider a bright blob at the jet origin (core) at time $t = 0$. After a time t it has moved along the jet. The transverse displacement is $\beta ct \sin\theta$ (see figure below). However, because the approaching blob is now closer to the observer by a distance $\beta c \cos\theta$, the observer measures a shorter time: $t' = t - \beta t \cos\theta$ and hence an apparent transverse velocity

$$\beta_{\rm T} = \frac{\beta \sin\theta}{1 - \beta\cos\theta} \qquad (1)$$

This gives $\beta_{\rm T} > 1$ when $\beta \simeq 1$ and θ is not too close to 90°.

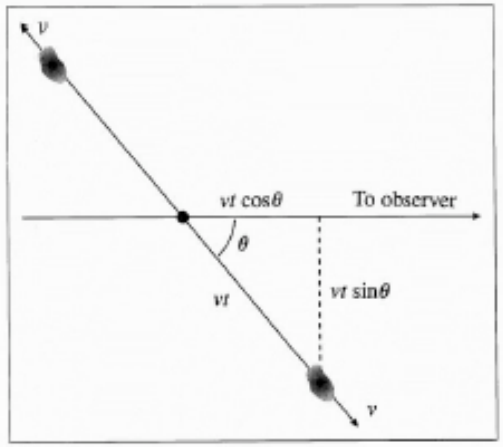

J. M. Paredes (2005)

Microquasars (HMXB)

Table 1 Microquasars in our Galaxy

Name	Position (J2000.0)	System type[a]	D (kpc)	P_{orb} (d)	$M_{compact}$ ($M_\odot$)	Activity radio[b]	β_{apar}	θ[c]	Jet size (AU)	Remarks[d]
High Mass X-ray Binaries (HMXB)										
LS I +61 303	$02^h40^m31^s.66$ $+61°13'45''.6$	B0V +NS?	2.0	26.5	–	p	$\geq$0.4	–	10–700	Prec?
V4641 Sgr	$18^h19^m21^s.48$ $-25°25'36''.0$	B9III +BH	~ 10	2.8	9.6	t	≥ 9.5	–	–	
LS 5039	$18^h26^m15^s.05$ $-14°50'54''.24$	O6.5V((f)) +NS?	2.9	4.4	1–3	p	≥ 0.15	$< 81°$	10–1000	Prec?
SS 433	$19^h11^m49^s.6$ $+04°58'58''$	evolved A? +BH?	4.8	13.1	11±5?	p	0.26	79°	$\sim 10^4$–10^6	Prec XRJ
Cygnus X-1	$19^h58^m21^s.68$ $+35°12'05''.8$	O9.7Iab +BH	2.5	5.6	10.1	p	–	40°	~ 40	
Cygnus X-3	$20^h32^m25^s.78$ $+40°57'28''.0$	WNe +BH?	9	0.2	–	p	0.69	73°	$\sim 10^4$	

Notes:
[a] NS: neutron star; BH: black hole.
[b] p: persistent; t:transient.
[c] jet inclination.
[d] Prec: precession; XRJ: X-ray jet.

J. M. Paredes (2005)

Microquasars (LMXB)

Table 1 Microquasars in our Galaxy

Name	Position (J2000.0)	System type[a]	D (kpc)	P_{orb} (d)	$M_{compact}$ ($M_\odot$)	Activity radio[b]	β_{apar}	θ[c]	Jet size (AU)	Remarks[d]
Low Mass X-ray Binaries (LMXB)										
Circinus X-1	$15^h20^m40^s.9$ $-57°10'01''$	Subgiant +NS	5.5	16.6	–	t	> 15	$< 6°$	$> 10^4$	
XTE J1550−564	$15^h50^m58^s.70$ $-56°28'35''.2$	G8−K5V +BH	5.3	1.5	9.4	t	> 2	–	$\sim 10^3$	XRJ
Scorpius X-1	$16^h19^m55^s.1$ $-15°38'25''$	Subgiant +NS	2.8	0.8	1.4	p	0.68	44°	~ 40	
GRO J1655−40	$16^h54^m00^s.25$ $-39°50'45''.0$	F5IV +BH	3.2	2.6	7.02	t	1.1	72°−85°	8000	Prec?
GX 339−4	$17^h02^m49^s.5$ $-48°47'23''$	– +BH	> 6	1.76	5.8±0.5	t	–	–	< 4000	
1E 1740.7−2942	$17^h43^m54^s.83$ $-29°44'42''.60$	– +BH ?	8.5?	12.5?	–	p	–	–	$\sim 10^6$	
XTE J1748−288	$17^h48^m05^s.06$ $-28°28'25''.8$	– +BH?	≥ 8	?	> 4.5?	t	1.3	–	$> 10^4$	
GRS 1758−258	$18^h01^m12^s.40$ $-25°44'36''.1$	– +BH ?	8.5?	18.5?	–	p	–	–	$\sim 10^6$	
GRS 1915+105	$19^h15^m11^s.55$ $+10°56'44''.7$	K−M III +BH	12.5	33.5	14±4	t	1.2−1.7	66°−70°	~ 10−10^4	Prec?

Notes:
[a] NS: neutron star; BH: black hole.
[b] p: persistent; t:transient.
[c] jet inclination.
[d] Prec: precession; XRJ: X-ray jet.

http://www.physics.usyd.edu.au/~kuncic/

Model of XRBs

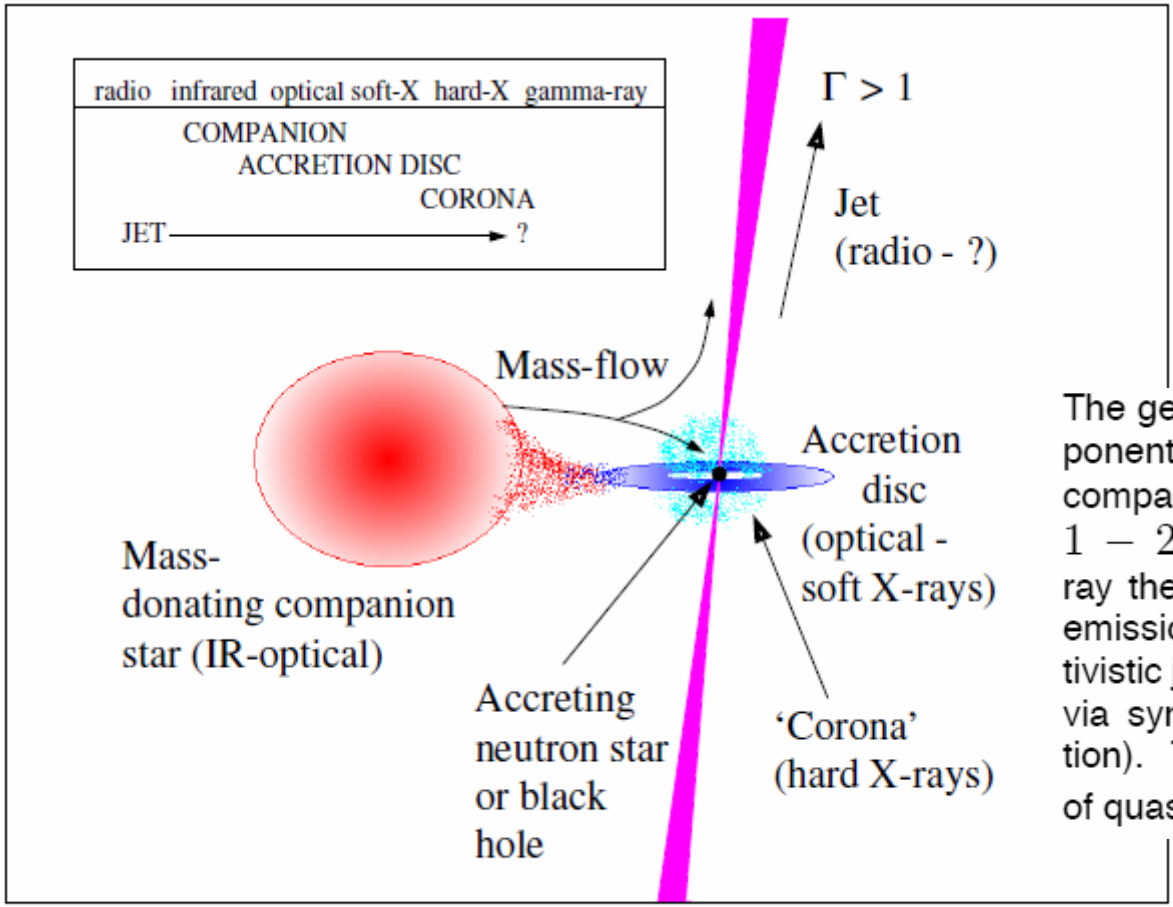

The generalised picture of XRBs: essential components are a companion star (mass-donor), compact stellar-mass object (WD/NS/BH, $M \simeq 1 - 20 M_\odot$), accretion disk (optical-to-soft X-ray thermal emission), corona (power-law X-ray emission via thermal Comptonisation), and relativistic jets (nonthermal hard X-ray/γ-ray emission via synchrotron, SSC, nonthermal Comptonisation). These systems are scaled-down versions of quasars (with $M \sim 10^{6-9} M_\odot$).

Fig. 3 Different components of a microquasars. From Fender & Macarone (2004).

http://www.physics.usyd.edu.au/~kuncic/

Vs. Quasar

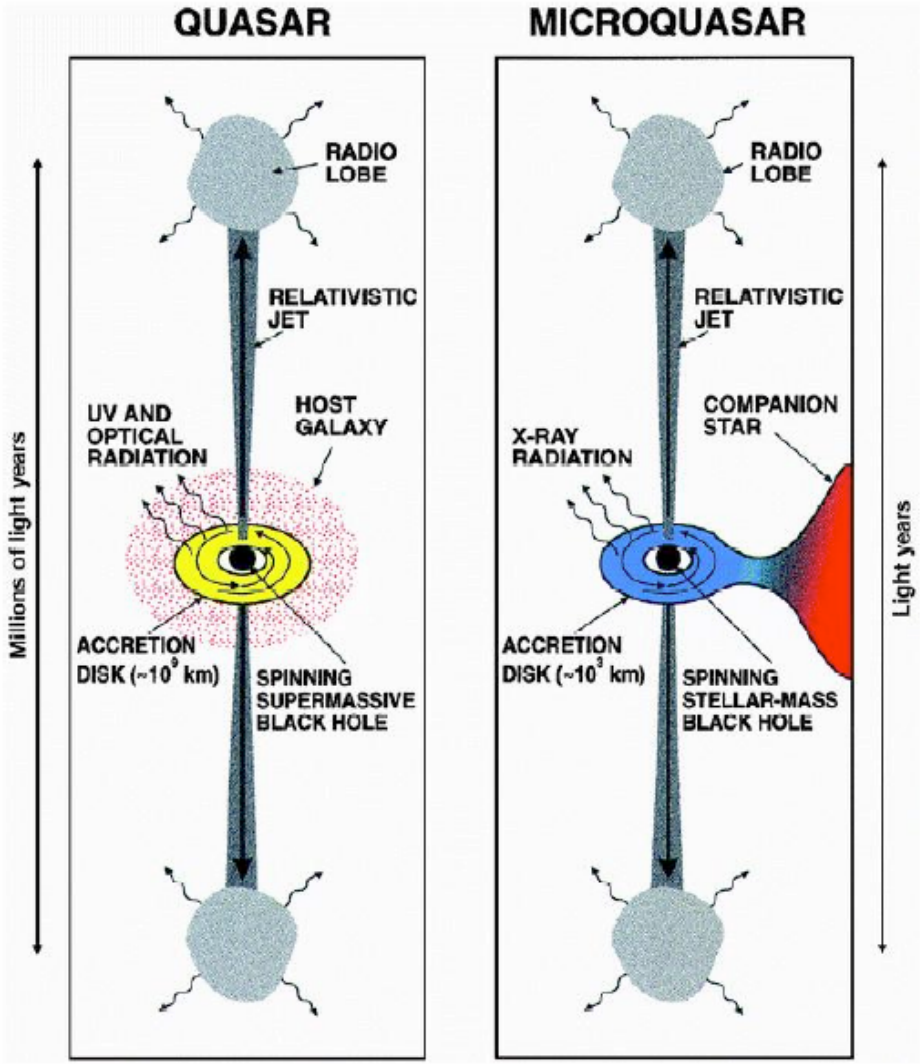

J. M. Paredes (2005)

High energy emission: observation

Table 2 High energy emission from microquasars

Name	INTEGRAL[a]		BATSE[b]		COMPTEL[c]	EGRET[d]	Others[e]
	30−50 keV (significance)	40−100 keV (count/s)	20−100 keV (significance)	160−430 keV (mCrab)	1−30 MeV (GRO)	> 100 MeV (3EG)	
High Mass X-ray Binaries (HMXB)							
LS I +61 303	–	–	5.2	5.1±2.1	J0241+6119?	J0241+6103?	
V4641 Sgr	–	–	–	–	–	–	
LS 5039	–	–	10.7	3.7±1.8	J1823−12?	J1824−1514?	
SS 433	13.5	<1.02	21.7	0.0±2.8	–	–	
Cygnus X-1	676.6	66.4±0.1	1186.8	924.5±2.5	yes	–	S
Cygnus X-3	122.7	5.7±0.1	197.8	15.5±2.1	–	–	O, T?
Low Mass X-ray Binaries (LMXB)							
Circinus X-1	–	–	3.8	0.3±2.6	–	–	
XTE J1550−564	8.6	0.6±0.07	17.1	−2.3±2.5	–	–	
Scorpius X-1	111.6	2.3±0.1	460.6	9.9±2.2	–	–	
GRO J1655−40	–	–	40.6	23.4±3.9	–	–	O
GX 339−4	21.9	0.55±0.03	89.0	580±3.5	–	–	S
1E 1740.7−2942	147.3	4.32±0.03	92.4	61.2±3.7	–	–	S
XTE J1748−288	–	–	−12.4	–	–	–	S
GRS 1758−258	135.9	3.92±0.03	74.3	38.0±3.0	–	–	S
GRS 1915+105	144.9	8.63±0.13	208.8	33.5±2.7	–	–	S, T?

Notes:

[a] The first IBIS/ISGRI soft gamma-ray galactic plane survey catalog (Bird et al. 2004).

[b] BATSE Earth occultation catalog, Deep sample results (Harmon et al. 2004).

[c] The first COMPTEL source catalogue (Schönfelder et al. 2000).

[d] The third EGRET catalog of high-energy γ-ray sources (Hartman et al. 1999).

[e] S: SIGMA instrument onboard GRANAT satellite; O: OSSE; T: TeV source.

G. E. Romero (2005)

Leptonic model (1)

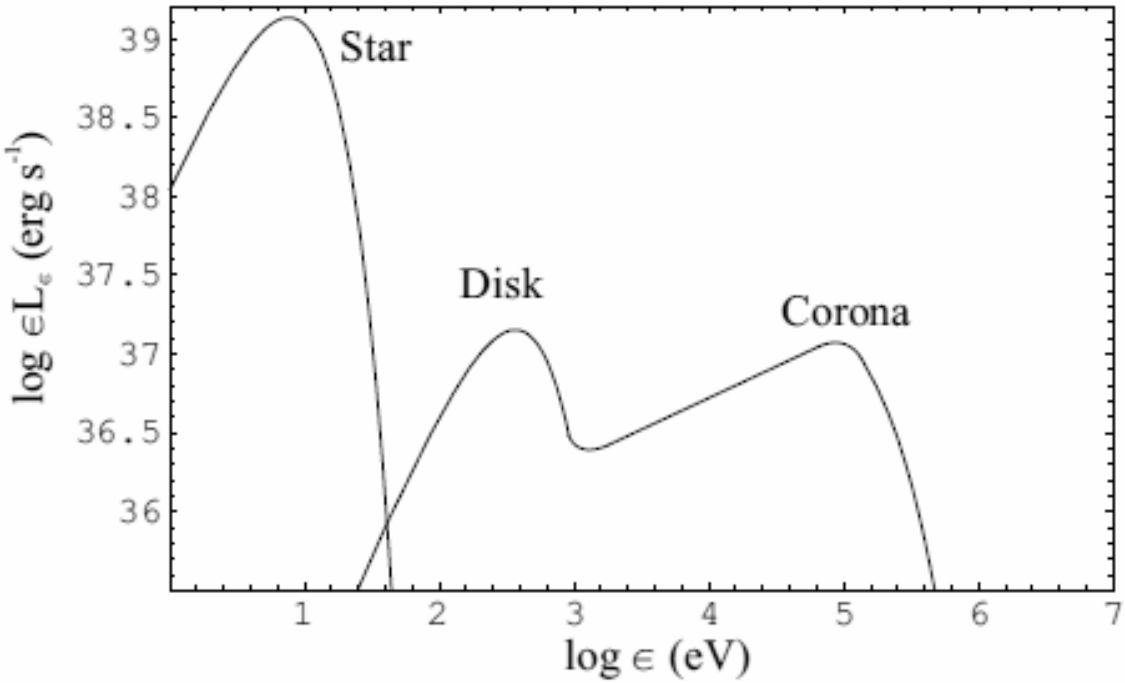

Fig. 4 External photon fields to which the jet is exposed in a microquasar with a high-mass companion.

G. E. Romero (2005)

Leptonic model (2)

Table 6. Parameters for a 'realistic' case.

Parameter (symbol)	Value
Corona luminosity ($L_{\rm cor}$)	3×10^{32} erg s^{-1}
Magnetic field ($B(z_0)$)	200 G
Maximum electron Lorentz factor ($\gamma_{\rm emax}(z_0)$)	10^4
Jet bulk Lorentz factor ($\Gamma_{\rm jet}$)	1.1
Viewing angle to jet's axis θ	10°
Disk/jet coupling constant ($q_{\rm e}$)	10^{-3}

Parameter (symbol)	Value
Black hole mass ($M_{\rm bh}$)	$10M_\odot$
Gravitational radius ($R_{\rm g}$)	1.48×10^6 cm
Accretion luminosity ($L_{\rm acc}$)	$10^{-8}\ M_\odot c^2$ year^{-1}
Stellar radius ($R_\star$)	$15\ R_\odot$
Stellar bolometric luminosity ($L_\star$)	5×10^{38} erg s^{-1}
Viewing angle to jet's axis θ	10°
Distance from jet's apex to the compact object (z_0)	$50\ R_{\rm g}$
Initial jet radius (R_0)	$0.1z_0$
Orbital radius ($R_{\rm orb}$)	$45\ R_\odot$
Peak energy of the disk ($kT_{\rm disk}$)	1 keV
Peak energy of the corona	150 keV
Peak energy of the star ($kT_{\rm star}$)	10 eV
Expansion coefficient of the jet (ε)	1
Minimum Lorentz factor for electrons in the jet (jet frame) ($\gamma_{\rm emin}$)	~1
Maximum Lorentz factor for electrons in the jet (jet frame) ($\gamma_{\rm emax}$)	10^4
Electron energy distribution power-law index (p)	2
Photon index for the corona ($\Gamma_{\rm cor}$)	1.6
Total disk luminosity ($L_{\rm disk}$)	10^{37} erg s^{-1}

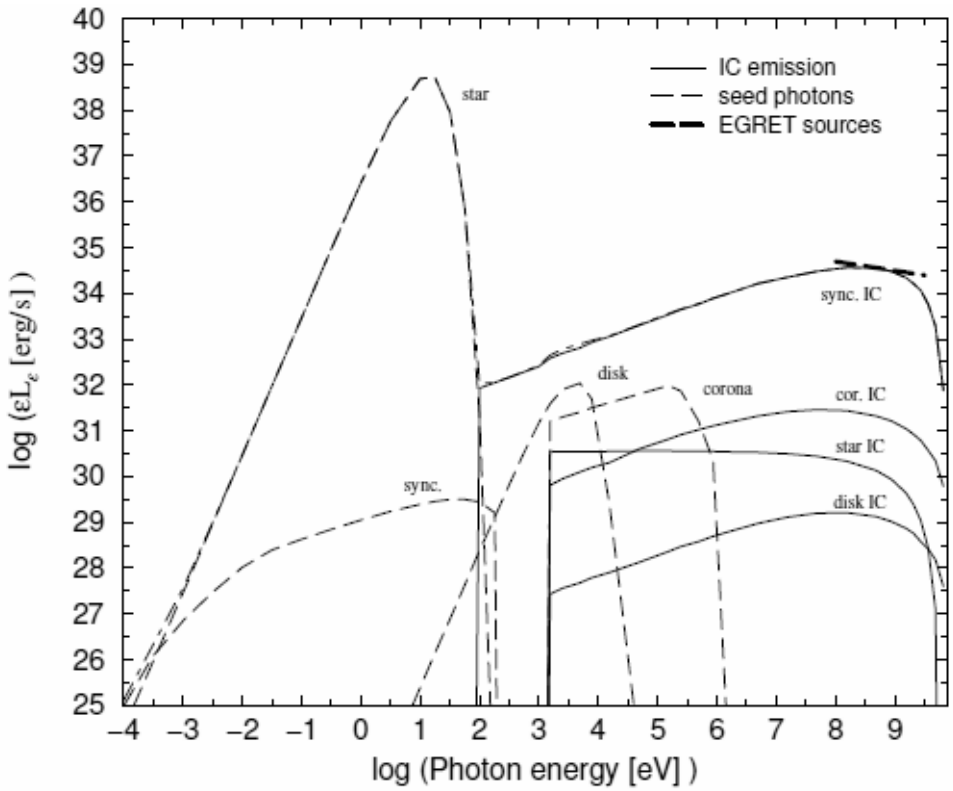

Fig. 5 Spectral energy distribution for a microquasar with an inhomogeneous leptonic jet, dominated by SSC losses. External Compton contributions from interactions between the jet and the stellar, disk and corona photon fields are also shown. From Bosch-Ramon et al. (2004).

G. E. Romero (2005)

Hadronic model

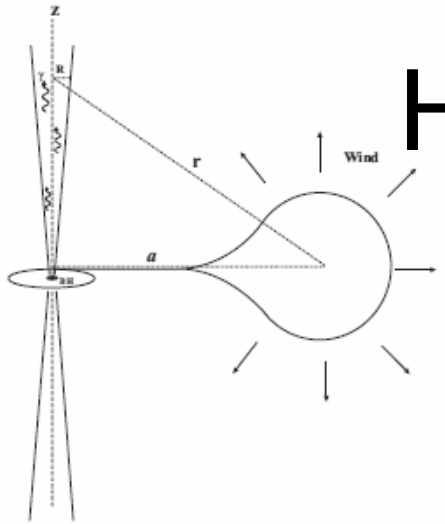

Fig. 1. Sketch of the general situation discussed in the paper. A relativistic $e - p$ jet is injected close to the black hole in a MQ with a high-mass stellar companion. The jet must traverse the matter field created by the stellar wind. The resulting interaction produces gamma-ray emission. In the figure perpendicularity is assumed between the jet and the orbital plane, but this particular assumption can be relaxed in a more general situation.

Table 1. Basic parameters of the model.

Parameter	Symbol	Value
Type of jet	ϵ	1
Black hole mass	$M_{\rm bh}$	10 $M_\odot$
Injection point	z_0	50 $R_{\rm g}^1$
Initial radius	R_0	5 $R_{\rm g}$
Radius of the companion star	r_*	35 $R_\odot$
Mass loss rate	$\dot{M}_*$	10^{-5} $M_\odot$ yr^{-1}
Terminal wind velocity	v_∞	2500 km s^{-1}
Black hole accretion rate	$\dot{M}_{\rm disk}$	10^{-8} $M_\odot$ yr^{-1}
Wind velocity index	β	1
Jet's expansion index	n	2
Jet's Lorentz factor	Γ	5
Minimum proton energy	$E_p^{\rm min}$	10 GeV
Maximum proton energy	$E_p^{\rm max}$	100 TeV
Orbital radius	a	2 r_*

[1] $R_{\rm g} = GM_{\rm bh}/c^2$.

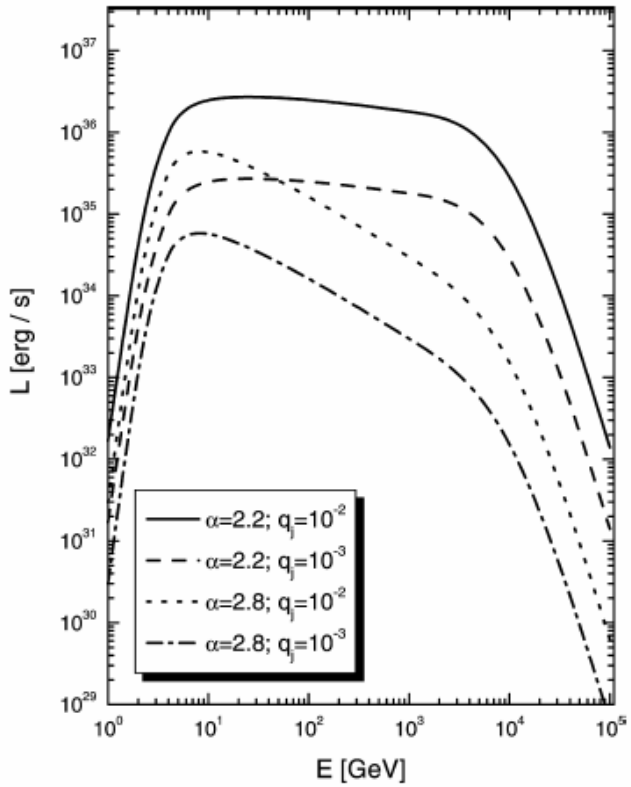

Fig. 7 Hadronic gamma-ray spectral energy distribution for a microquasar with a massive (O9 I) stellar companion. Different curves correspond to different jet/disk coupling constant $q_{\rm j}$ and proton spectral index α. The viewing angle of the jet is 10 degrees. From Romero et al. (2003).

http://www.physics.usyd.edu.au/~kuncic/

LS5039 by H.E.S.S. (1)

We should expect to occasionally see jets "pole on", rather than in projection on the sky. By direct analogy with blazars, microblazars are expected to be exceptionally bright, point-like, and highly variable sources of hard X-ray and γ-ray emission. A few candidate microblazars have been found in our galaxy, including the $\gtrsim 100$ GeV source LS 5039 detected by the HESS γ-ray satellite (Aharonian et al. 2005, *Science Express*)

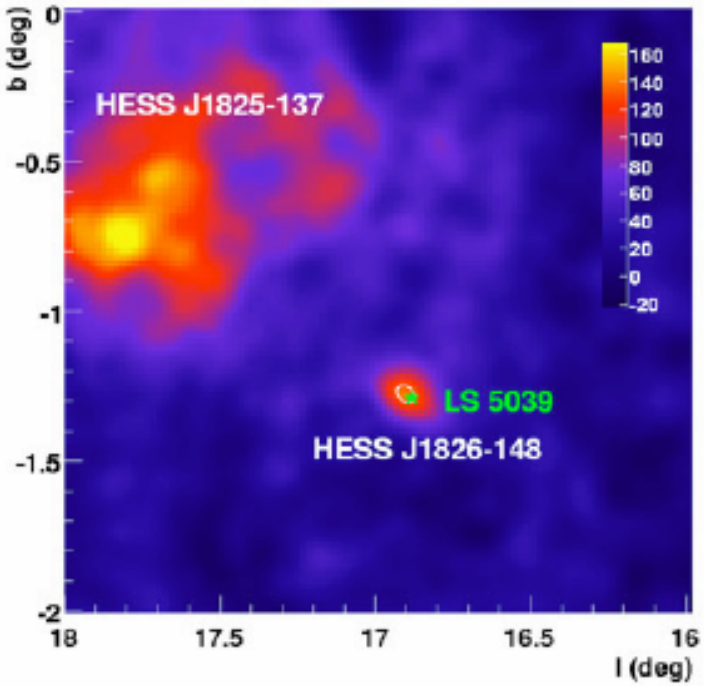

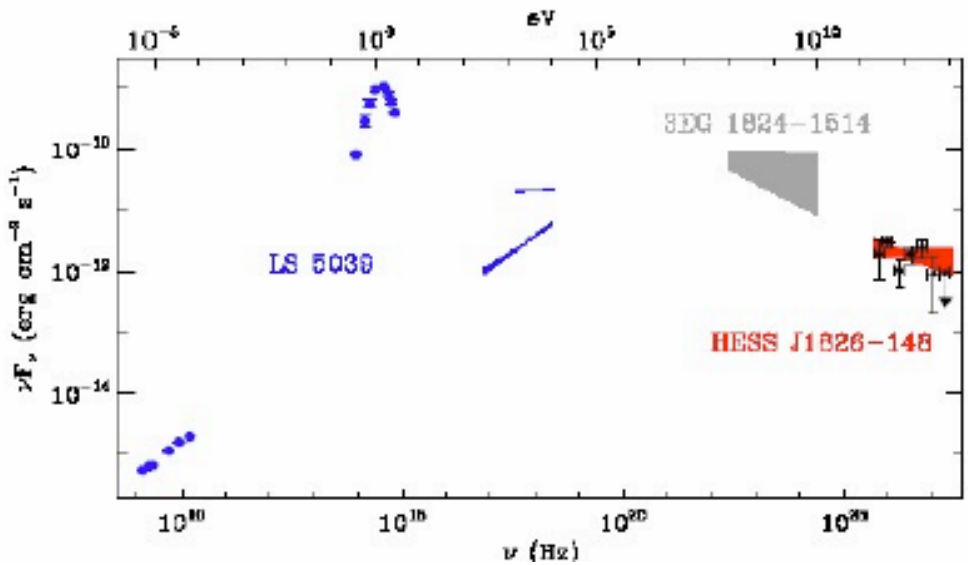

Aharonian et al., astro-ph/0607192

LS5039 by H.E.S.S. (2)

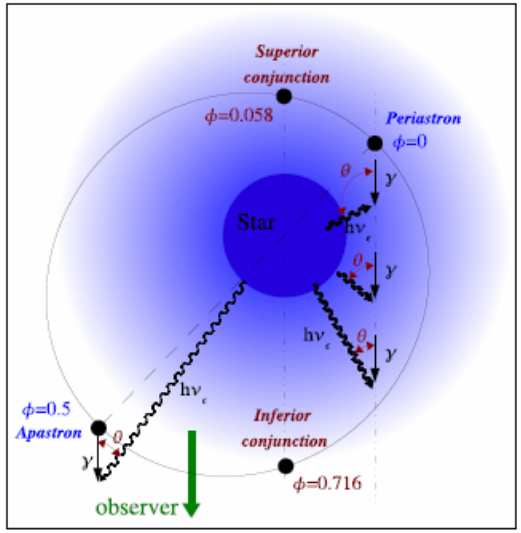

Fig. 4. The orbital geometry (Casares et al. 2005) viewed from directly above LS 5039. Shown are: phases (ϕ) of minimum (periastron) and maximum (apastron) separation between the two components; epochs of superior and inferior conjunctions of the compact object representing phases of co-aligment along our line-of-sight of the compact object and stellar companion. The orbit is actually inclined at an angle in the range $13° < i < 64°$ with respect to the view above. VHE γ-rays (straight black lines with arrows) can be absorbed by optical photons of energy $h\nu_\epsilon$, when their scattering angle θ exceeds zero.

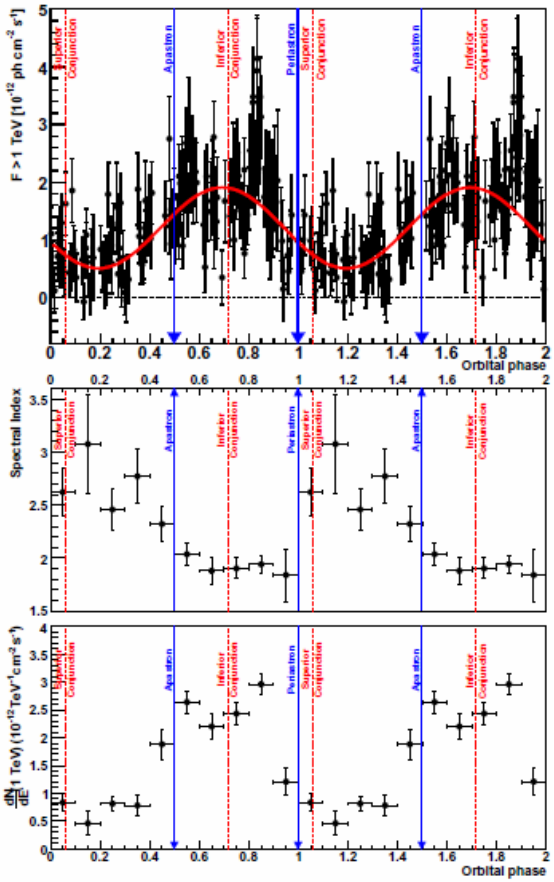

Fig. 5. Top: Integral γ-ray flux ($F > 1$ TeV) lightcurve (phasogram) of LS 5039 from HESS data (2004 to 2005) on a run-by-run basis folded with the orbital ephemeris of Casares et al. (2005). Each run is ~28 minutes. Two full phase (ϕ) periods are shown for clarity. The blue solid arrows depict periastron and apastron. The thin red dashed lines represent the superior and inferior conjunctions of the compact object, and the thick red dashed line depicts the Lomb-Scargle Sine coefficients for the period giving the highest Lomb-Scargle power. This coefficient is subtracted from the light curve in Fig 1 middle panel.

Aharonian et al., astro-ph/0607192

LS5039 by H.E.S.S. (3)

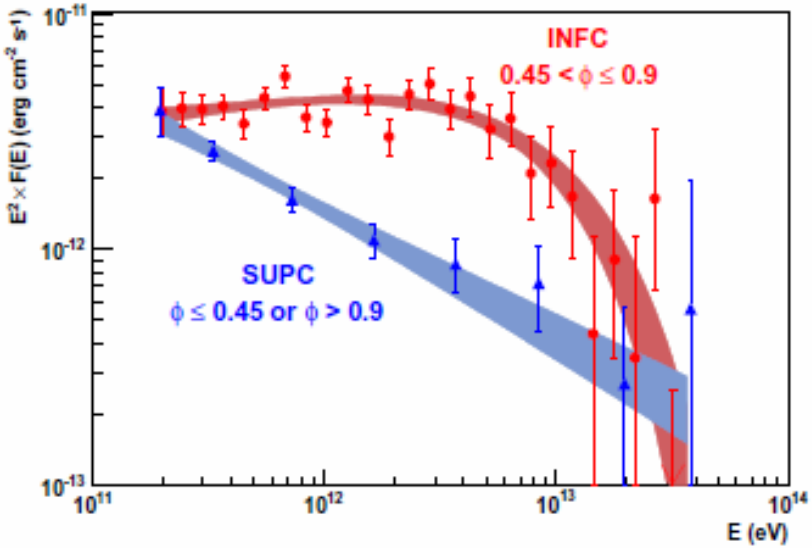

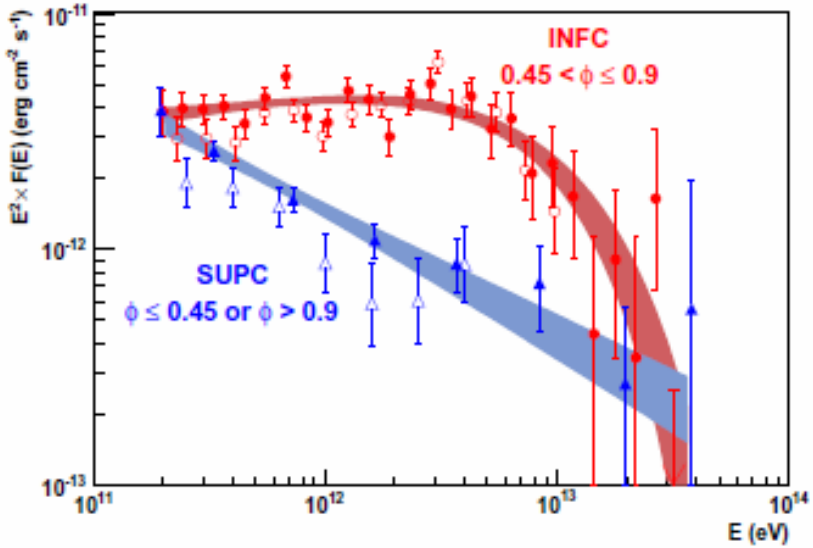

Fig. 6. Very high energy γ-ray spectra of LS 5039 for two broad orbital phase intervals (defined in the text): **INFC** $0.45 < \phi \leq 0.9$ (red circles); **SUPC** $\phi \leq 0.45$ or $\phi > 0.9$ (blue triangles). The shaded regions represent the 1σ confidence bands on the fitted functions (Tab. 1). Both spectra are mutually incompatible with the probability that the same spectral shape would fit both simultaneously being $\sim 2 \times 10^{-6}$. A clear spectral hardening in the region 0.3 to $\sim$ 20 TeV is noticed for the **INFC** phase interval.

Fig. 8. Energy spectra of LS 5039 separated into the same broad phase intervals as for Fig. 6. **INFC** $0.45 < \phi \leq 0.9$ (red circles); **SUPC** $\phi \leq 0.45$ or $\phi > 0.9$ (blue triangles), comparing results from the semi-analytical Model+Hillas (filled markers) and Hillas-only (open markers) analyses (Aharonian et al. 2006), respectively. The Hillas-only analysis has made use of an independent calibration chain.

Bosch-Ramon et al., astro-ph/0605466

Leptonic model of LS5039

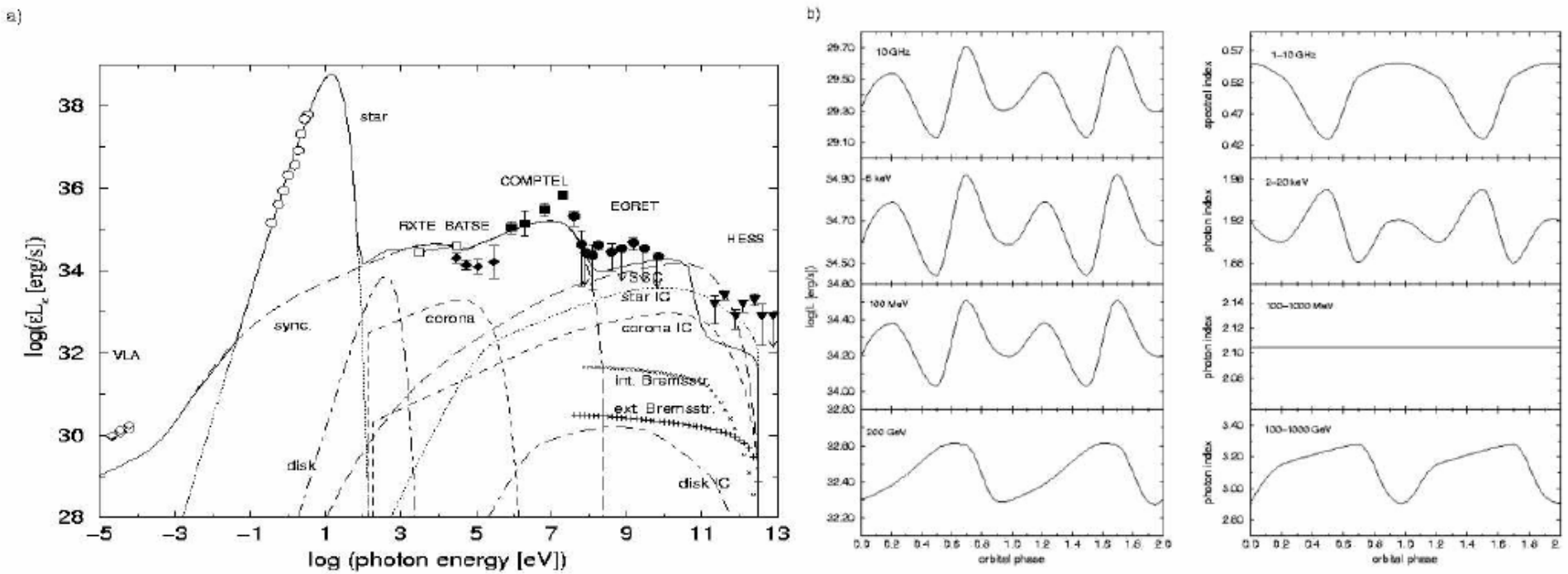

Figure 1. a) Computed SED for LS 5039 and b) its flux and photon index evolution at different energy bands.

Albert et al., Science 312 (2006) 1771

LSI+61 303 by MAGIC (1)

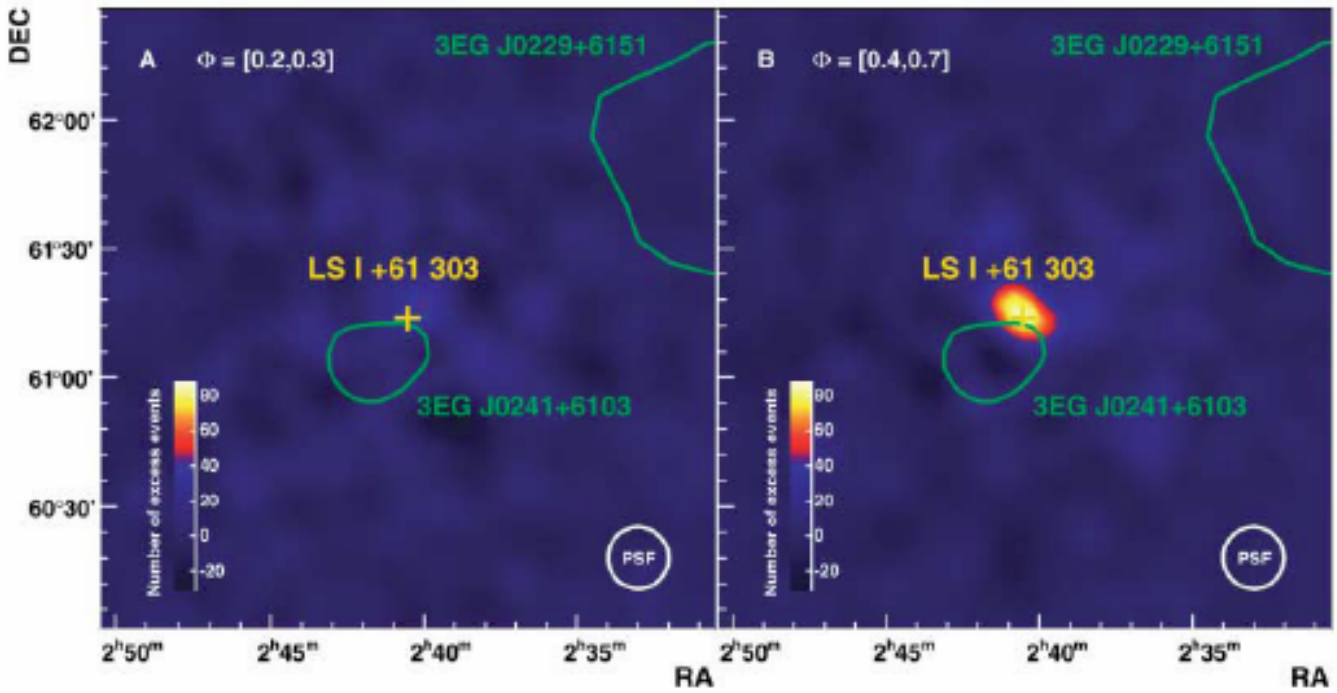

Fig. 1. Smoothed maps of gamma-ray excess events above 400 GeV around LS I +61 303. (**A**) Observations over 15.5 hours corresponding to data around periastron (i.e., between orbital phases 0.2 and 0.3). (**B**) Observations over 10.7 hours at orbital phase between 0.4 and 0.7. The number of events is normalized in both cases to 10.7 hours of observation. The position of the optical source LSI +61 303 (yellow cross) and the 95% confidence level contours for 3EG J0229+6151 and 3EG J0241+6103 (green contours) are also shown. The bottom right circle shows the size of the point spread function of MAGIC (1σ radius). No significant excess in the number of gamma-ray events is detected around periastron passage, whereas it shows up clearly (9.4σ statistical significance) at later orbital phases, in the location of LS I +61 303.

Albert et al., Science 312 (2006) 1771

LSI+61 303 by MAGIC (2)

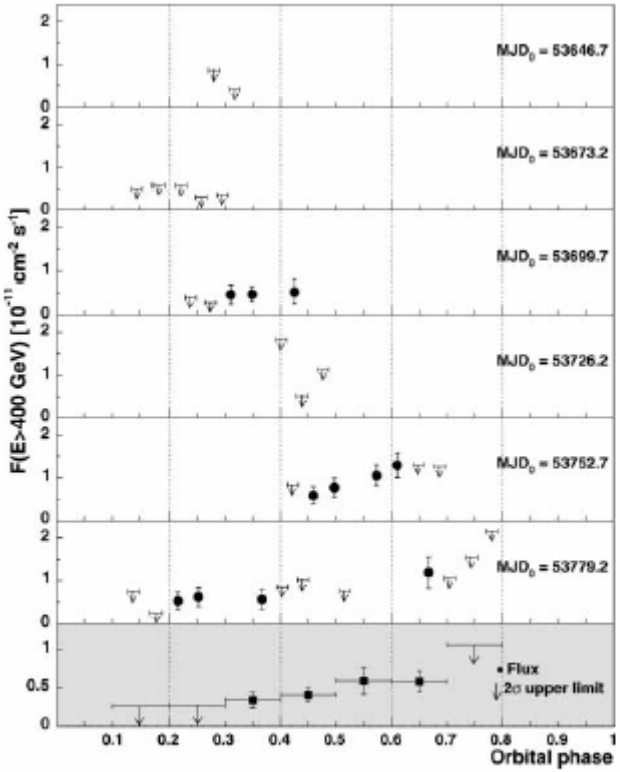

Fig. 2. VHE gamma-ray flux of LS I +61 303 as a function of orbital phase for the six observed orbital cycles (six upper panels, one point per observation night) and averaged for the entire observation time (bottom panel). Vertical error bars include 1σ statistical error and 10% systematic uncertainty on day-to-day relative fluxes. Only data points with more than 2σ significance are shown, and 2σ upper limits (*33*) are derived for the rest. The modified Julian date (MJD) corresponding to orbital phase 0 is indicated for every orbital cycle. The orbital phase is computed with orbital period of 26.4960 days and zero phase at JD 2443366.775 (*9*); periastron takes place at phase 0.23 (*10*). Marginal detections occur between orbital phases 0.2 and 0.4 in different cycles, whereas a significant increase of flux is detected from phase ~0.45 to phase ~0.65 in the fifth cycle, peaking at ~16% of the Crab Nebula flux on MJD 53769 (phase 0.61). During the following cycle, the highest flux is measured on MJD 53797 (phase 0.67). This behavior suggests that the VHE gamma-ray emission from LS I +61 303 has a periodic nature.

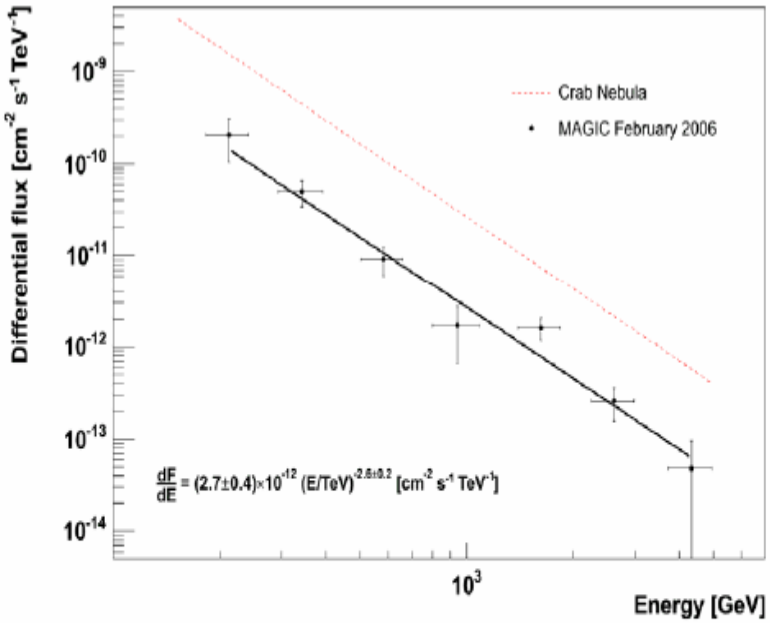

Fig. S2. Differential energy spectrum measured for LS I +61 303 for orbital phases between 0.4 and 0.7 and energies between 200 GeV and 4 TeV. The error bars show the 1σ statistical uncertainty. The dashed, red line corresponds to the Crab Nebula differential spectrum measured by MAGIC. The solid, black line is a fit of a power law (also expressed mathematically in the inset) to the measured points.

Dubus, A&A 451 (2006) 9

Gamma-ray absorption (1)

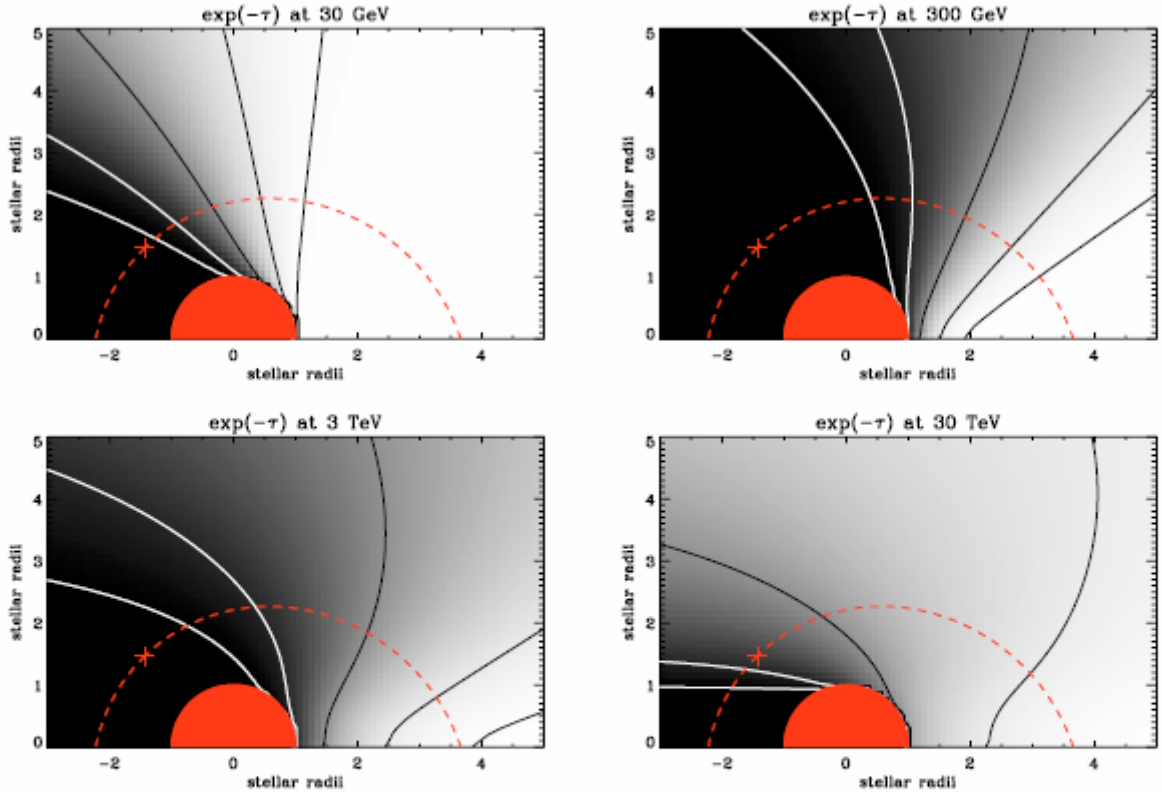

Fig. 1. Gamma-ray absorption map around a massive star. The grey-scale at each location corresponds to the integrated $\gamma\gamma$ absorption seen by a VHE photon emitted at this location and travelling in the plane of this figure towards an observer located at infinity to the right. The plotted value is $\exp(-\tau_{\gamma\gamma})$, on a linear scale with black corresponding to high absorption and white to low absorption. Absorption is shown for VHE photons with energies of 30 GeV, 300 GeV, 3 TeV and 30 TeV. Full lines are contours corresponding to 99%, 90% (white), 50%, 10% and 1% (black) of the emitted flux being absorbed. The star is located at the origin, has a 10 $R_\odot$ radius and an effective temperature of 40 000 K. The orbit of the binary system LS 5039 is (partially) shown as a dotted line for illustrative purposes. Here, the binary would be seen edge-on ($i = 90°$) by the observer at right. Gamma-rays emitted close to the compact object towards this observer are more or less absorbed according to orbital phase, with maximum absorption occurring after periastron (marked by a cross). The resulting flux modulation would be close to that shown in Fig. 2 for the case of $i = 60°$.

Dubus, A&A 451 (2006) 9

Gamma-ray absorption (2)

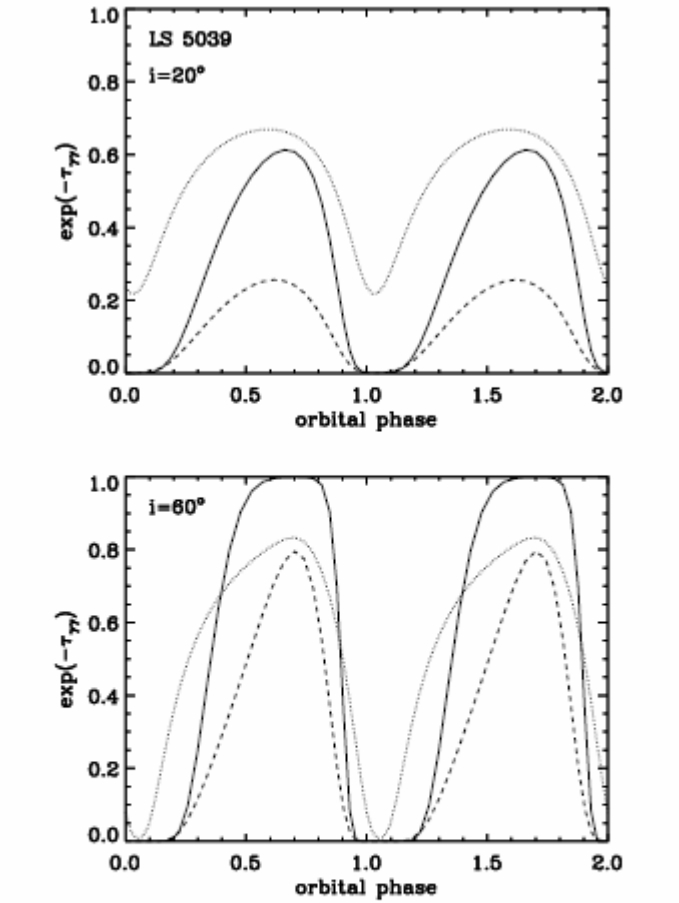

Fig. 2. Modulation of the γ-ray transmission $\exp(-\tau_{\gamma\gamma})$ with orbital phase in LS 5039 for two values of the system inclination i. A canonical neutron star corresponds to $i = 60°$ while $i = 20°$ implies a 4.5 $M_\odot$ black hole. Isotropic γ-ray emission is assumed to occur at the location of the compact object. The solid line is for 100 GeV photons (HESS threshold), dashed is for 1 TeV and dotted for 10 TeV photons. Periastron passage is at $\phi = 0$.

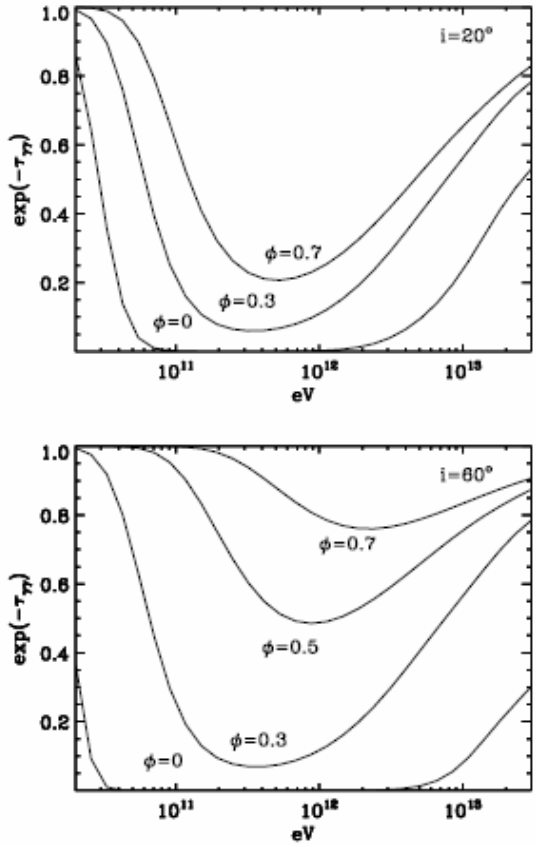

Fig. 4. Spectrum of γ-ray absorption at selected orbital phases ϕ for two inclinations i of LS 5039 (see Fig. 2). The absorption spectrum varies little for $i = 20°$. The line-like absorption feature may therefore be easier to detect for low inclinations, despite the stronger absorption near periastron for $i = 60°$. In the latter case, although spectral variations will be easier to detect, the large differences in absorption spectrum can swamp out the line feature in a phase-averaged spectrum. An almost absorption-free view of the intrinsic spectrum is expected at flux maximum for $i = 60°$.

Bednarek, MNRAS 368 (2006) 579

Cascading gamma-rays (1)

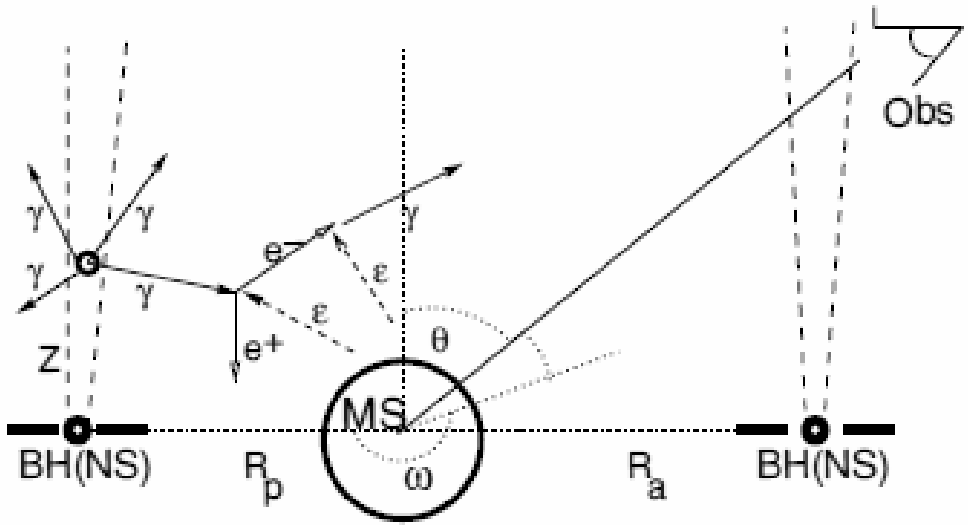

Figure 1. Schematic picture of a compact binary system composed of a massive star and a compact object (a black hole or a neutron star) on an orbit around the massive OB star. The observer is located at the inclination angle θ and the azimuthal angle ω. The matter accreting on to a compact object from the massive star creates an accretion disc. Particles (electrons or protons) are accelerated inside the jet launched from the inner part of an accretion disc. Primary electrons and/or γ-rays, injected at the distance z from the base of the jet, initiate an anisotropic IC $e^{\pm}$ pair cascade in the radiation field of the massive star. A part of the primary γ-rays and secondary cascade γ-rays escapes from the binary system towards the observer.

Bednarek, MNRAS 368 (2006) 579

Cascading gamma-rays (2)

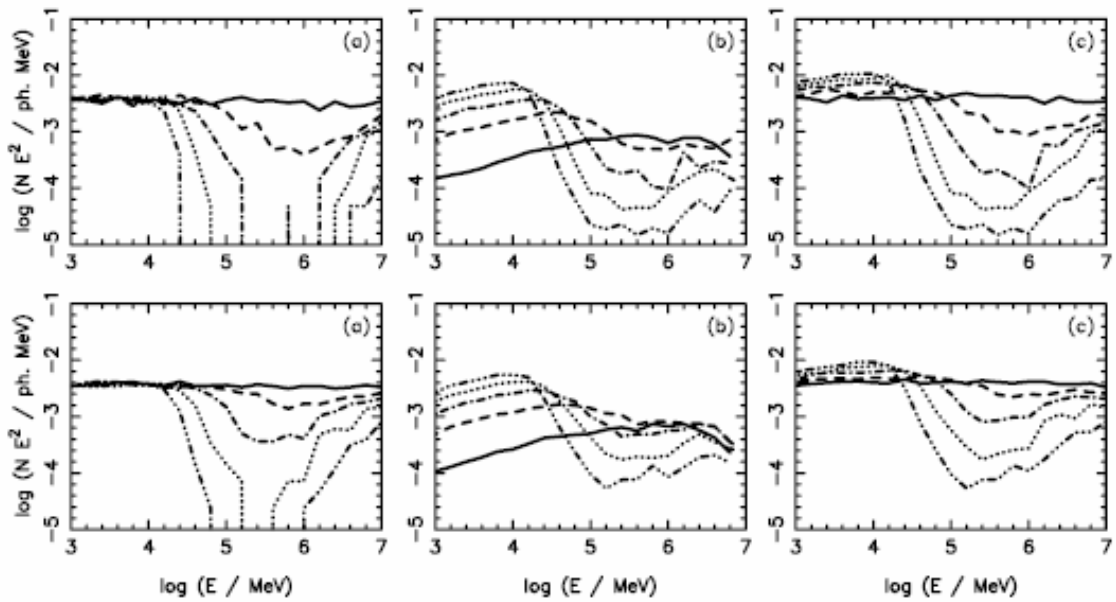

Figure 3. Differential γ-ray spectra (multiplied by the square of photon energy) escaping from the binary system at a specific range of the cosine angles α, measured with respect to the direction defined by the injection place and the centre of the massive star. The range of $\Delta \cos\alpha$ (with the width 0.1) is centred on 0.95 (full curve), 0.55 (dashed), 0.15 (dot–dashed), -0.25 (dotted) and -0.65 (triple-dot–dashed). γ-rays are produced in the cascade initiated by primary γ-rays with the power-law spectrum and spectral index 2 which are injected isotropically close to the base of the jet ($z \approx 0 \ll r_\star$, but sufficiently far away from the accretion disc), and at two distances from the massive star $2.2r_\star$ (upper figures, corresponding to the periastron passage of the compact object) and $4.5r_\star$ (bottom figures, corresponding to the apastron passage). (a) Spectra of primary γ-rays escaping without interaction. (b) Spectra of secondary γ-rays produced in the IC cascade. (c) Total spectra of γ-rays escaping from the binary system [the sum of spectra shown in (a) and (b)].

Bednarek, MNRAS 368 (2006) 579

Cascading gamma-rays (3)

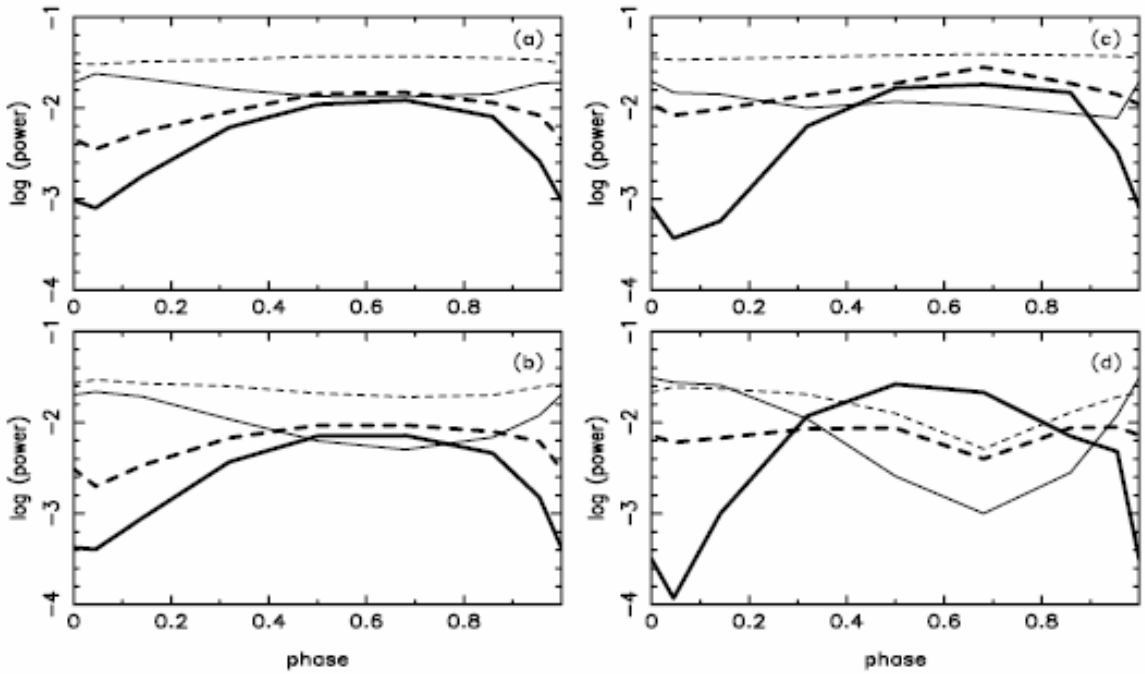

Figure 9. The power in γ-rays which escape from the binary system LS 5039 towards the observer (the γ-ray light curve) at the inclination angle $\theta = 25°$ (a and b) and $\theta = 60°$ (c and d), for the case of isotropic injection of primary γ-rays (a and c) and primary electrons (b and d), as a function of the phase of the injection place of the primary particles (*phase* is the time measured from the periastron passage divided by the orbital period of the binary system) at photon energies in the range 1–10 GeV (thin curves) and above 100 GeV (thick curves). The injection place of primary particles occurs in the jet. The light curves are shown for the injection place at the base of the jet $z \approx 0 r_\star$ (full curves) and at the distance $5 r_\star$ along the jet (dashed curve).

Summary

- Microquasars are good candidates for VHE gamma-ray sources.
- Both leptonic and hadronic models can be accomodated to fit the spectrum below ~GeV.
- Recently two VHE sources were found: LS 5039 and LSI +61 303. Their gamma-ray fluxes show orbital variation. This may be related to gamma-ray opacities around the binary system. In that case there will be a feature in the energy spectrum.